International Journal of Nanomedicine

Dovepress
Taylor & Francis Group

Open Access Full Text Article

ORIGINAL RESEARCH

A Photothermally Triggered Nanoplatform for Multidimensional Antibacterial Therapy and Accelerated Healing of Infected Wounds

Yueying Fan[1,*], Jinfu Li[1,*], Peng Wang[1,*], Yuhuan Peng[1], Chao Yan[1], Xiangyang Li[1], Zhaoxiang Wang[1], Xiao Li[1], Zhanchen He[1], Wenqiang Li[2], Bin Yin[1], Chiyu Jia[1]

[1]Center of Burn & Plastic and Wound Healing Surgery, The First Affiliated Hospital of University of South China, Hengyang Medical School, University of South China, Hengyang, Hunan, 421001, People's Republic of China; [2]Guangdong Traditional Medical and Sports Injury Rehabilitation Research Institute, The Affiliated Guangdong Second Provincial General Hospital of Jinan University, Guangzhou, Guangdong 510317, People's Republic of China

*These authors contributed equally to this work

Correspondence: Bin Yin; Chiyu Jia, Email ybyinbin@126.com; jiachiyu309@163.com

Background: Bacterial infection and biofilm formation synergistically hinder wound healing by perpetuating inflammation and evading conventional treatments. Monotherapeutic strategies often fail to simultaneously eradicate resilient biofilms and rectify the dysregulated wound microenvironment. To overcome these limitations, we developed a multifunctional and targeted nanoplatform for synergistic antibacterial therapy and immunomodulation.

Methods: The smart nanoplatform (CCP-DFO(Fe)) was constructed with a triple-component architecture: a photothermal Cu_7S_4 core pre-loaded with chlorogenic acid (CGA), enveloped by a thermo-responsive poly(N-vinylcaprolactam) (PVCL) shell, and surface-functionalized with deferoxamine-iron (DFO(Fe)) via amide coupling for active bacterial targeting.

Results: The nanoplatform exhibits effective bacterial targeting via DFO(Fe)-mediated siderophore mimicry, enabling preferential accumulation at infection sites. Under NIR irradiation, CCP-DFO(Fe) nanoplatform exhibits efficient photothermal conversion, rapidly elevating the temperature to 44.3 °C within 4 min, which induces the sudden collapse of the PVCL shell from a uniform swollen state to a phase-separated state, leading to shell disruption and consequent exposure of the CGA-loaded Cu_7S_4 nanoparticles (CSC). Under physiological conditions, the CSC nanoplatform gradually releases Cu^{2+} and CGA, which, together with the photothermal effect, synergistically exert potent antibacterial activity. As a result, the nanoplatform achieves highly effective bacterial eradication, reducing the survival rates of both *E. coli* and *S. aureus* to below 5%, along with pronounced anti-biofilm activity. Beyond its antibacterial activity, the released CGA further exerts antioxidant and anti-inflammatory effects by scavenging reactive oxygen species and promoting macrophage polarization toward the pro-healing M2 phenotype, thereby facilitating inflammation resolution. In an infected rat wound model, CCP-DFO(Fe) combined with NIR irradiation achieved 98.56 ± 1.08% wound closure by day 14, with nearly complete bacterial eradication, while simultaneously promoting angiogenesis and collagen deposition.

Conclusion: This integrated nanoplatform combines targeted antibacterial activity, biofilm disruption, and inflammation resolution into a single system, demonstrating significant potential for treating infected and chronic wounds.

Keywords: smart nanoplatform, targeted antibacterial, photothermal therapy, infected wound healing

Introduction

The physiological healing of skin relies on the coordinated and sequential progression through four distinct yet overlapping phases: hemostasis, inflammation, proliferation, and remodeling.[1] However, bacterial infection severely disrupts this precisely orchestrated process, ultimately leading to impaired wound healing or even complete stagnation.[2–4] Pathogens, most notably *Staphylococcus aureus* (*S. aureus*), not only cause direct tissue damage via toxins and enzymes but, more critically, their persistence drives an excessive inflammatory response.[5] This results in aberrant neutrophil infiltration, polarization of macrophages toward the pro-inflammatory M1 phenotype, and the overproduction of reactive oxygen species

https://doi.org/10.2147/IJN.S594688
Received: 8 January 2026
Accepted: 24 April 2026
Published: 7 May 2026

Graphical Abstract

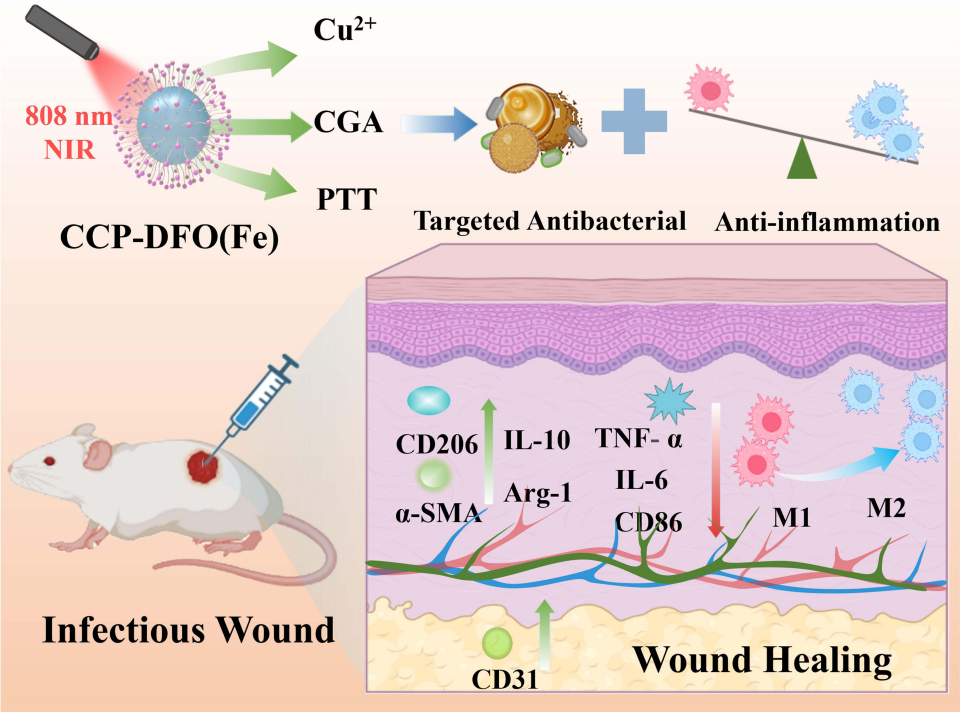

(ROS) and pro-inflammatory cytokines.[6,7] Such a dysregulated inflammatory microenvironment subsequently suppresses fibroblast proliferation and collagen synthesis while impairing vascular endothelial cell function, thereby hindering two pivotal healing events: re-epithelialization and angiogenesis.[8] Furthermore, the formation of bacterial biofilms provides an additional physical barrier, enhancing bacterial resistance and immune evasion[9,10.] Consequently, infected wounds often remain trapped in the inflammatory or early proliferative phase, failing to transition into the remodeling and maturation stages.[11] This is clinically manifested as delayed healing, recurrence, and a significantly elevated risk of chronicity.[12] Therefore, developing novel therapeutic strategies capable of effectively combating infection while precisely modulating the healing microenvironment represents an urgent clinical and scientific imperative.

Currently, the clinical management of infected wounds primarily relies on topical antimicrobial agents and systemic antibiotics. However, such approaches are generally constrained by a high propensity to induce bacterial resistance and limited ability to support the wound healing process.[13–15] Photothermal therapy (PTT) has emerged as a promising non-antibiotic strategy for infected wound management, owing to its deep tissue penetration and spatiotemporally controllable antibacterial activation.[16,17] The localized hyperthermia generated under near-infrared (NIR) irradiation can effectively inactivate bacteria while promoting microcirculation and facilitating drug release.[18–22] However, the antibacterial efficacy of PTT alone remains limited, especially as bacteria develop enhanced heat tolerance, rendering low-temperature hyperthermia often insufficient for complete bacterial eradication,[23] while excessive heating may cause collateral damage to surrounding healthy tissues.[24–26] Copper-based nanomaterials integrate Cu^{2+}-mediated antibacterial activity with NIR-responsive photothermal conversion, enabling membrane disruption, metabolic interference, and localized heat generation for effective infection control. For instance, recent studies have demonstrated the therapeutic potential of copper-based nanomaterials in infected wound management. Wu et al developed temperature-responsive copper-containing nanoassemblies for synergistic photothermal antibacterial activity,[27] while Zhou et al constructed copper-based nanoparticles that promoted bacterial eradication, tissue regeneration, and angiogenesis also through the synergistic action of Cu^{2+} and PTT.[28] However, despite these encouraging results, copper-based systems still face notable

limitations, including potential ion-associated cytotoxicity, limited biostability, and a lack of selective bacterial targeting.[29] To overcome the limitation of insufficient targeting, various strategies have been explored, although electrostatic and ligand- or antibody-mediated approaches often suffer from limited specificity, poor stability, or high cost.[30] In contrast, siderophore-mediated targeting exploits the intrinsic iron acquisition pathways of bacteria. Deferoxamine (DFO), a clinically approved iron chelator, can form DFO(Fe) complexes that mimic natural siderophores and are actively internalized by bacteria,[31] thereby enabling a "Trojan horse" strategy for targeted delivery.[30,32] Although the incorporation of DFO(Fe)-mediated targeting improves bacterial accumulation and specificity, challenges related to biosafety and the regulation of the inflammatory microenvironment still remain. In this context, the incorporation of biocompatible natural bioactive compounds into nanoplatforms offers an effective strategy to enhance biosafety while modulating the inflammatory microenvironment.

Chlorogenic acid (CGA), a natural polyphenol, exhibits potent antioxidant and anti-inflammatory properties.[33,34] At the cellular level, CGA modulates multiple inflammatory and redox-related signaling pathways, including NF-κB-, MAPK-, and JAK/STAT-associated cascades as well as Nrf2-dependent antioxidant signaling, thereby suppressing excessive inflammatory responses and promoting macrophage polarization toward the pro-healing M2 phenotype.[33,35,36] However, its clinical application is limited by low bioavailability, poor stability, and rapid clearance, hindering effective accumulation and sustained action at the infection site.[37] Owing to its multiple phenolic hydroxyl and carboxyl groups, CGA can coordinate with metal ions and serve as a functional component in nanomaterial construction.[38] Such coordination behavior has been widely exploited for constructing functional nanostructures. For instance, Liu et al synthesized chlorogenic acid-functionalized silver nanoparticles, where CGA served as a surface capping agent, significantly enhancing nanoparticle stability.[39] In another study, Fu et al developed a CGA-incorporated metal-organic systems can regulate metal ion release and reduce associated toxicity, thereby enhancing wound healing outcomes.[38] These findings suggest that integrating CGA into metal-based nanomaterials not only improves its bioavailability but also mitigates metal ion-associated cytotoxicity, ultimately enhancing overall therapeutic performance.

This study developed a photothermally controlled nanoplatform, CCP-DFO(Fe), which significantly enhances the healing of bacterially infected wounds through synergistic multidimensional antibacterial activity and anti-inflammatory, pro-healing effects. A hierarchical design (Figure 1) was employed, in which the architecture was constructed around a photothermally active Cu_7S_4 core loaded with the natural antibacterial and anti-inflammatory polyphenol CGA, coated with a thermosensitive poly(N-vinylcaprolactam) (PVCL) outer shell, which serves as a protective barrier that mitigates direct Cu^{2+} exposure and enhances structural stability while enabling temperature-responsive release behavior. Further surface functionalization via an amide reaction with DFO(Fe) conferred active bacterial targeting. Under near-infrared irradiation, Cu_7S_4 generates photothermal heating,[40,41] inducing a phase transition in the PVCL layer that triggers the release of CGA.[42,43] The released CGA primarily exerts antibacterial effects during the early infection stage and, in the healing phase, further modulates the inflammatory microenvironment by scavenging ROS and inducing macrophage polarization toward the M2 phenotype. The photothermal effect provided by Cu_7S_4 not only enhances bactericidal efficacy but also drives the on-demand release of CGA. Meanwhile, the surface-grafted DFO(Fe) moiety is specifically recognized by the bacterial iron-uptake system, guiding nanoparticle accumulation at the infection site, thereby improving antibacterial precision and reducing off-target toxicity.[32,44,45] The designed CCP-DFO(Fe) system achieves spatiotemporal regulation spanning from infection clearance to tissue reconstruction, offering a next-generation nanomedical solution for the precise treatment of complex infected wounds.

Methods and Materials

Materials

Cupric acetate anhydrous (98%), thiourea (99%), polyvinylpyrrolidone (PVP, Mw ~8000), chlorogenic acid (98%), N, N-dimethylacetamide (DMAc), N-vinylcaprolactam (NVCL), poly(ethylene glycol) methyl ether methacrylate (OEGMA, Mw~300), acrylic acid (AA, 98%), and deferoxamine mesylate (DFO) were purchased from Macklin Biochemical Technology Co., Ltd. (Shanghai). N,N′-methylenebisacrylamide (MBA, 98%) and 2,2′-azobis[2-(2-imidazolin-2-yl)propane] dihydrochloride (VA-044, 99%) were obtained from Shanghai Aladdin Biochemical Technology Co., Ltd.

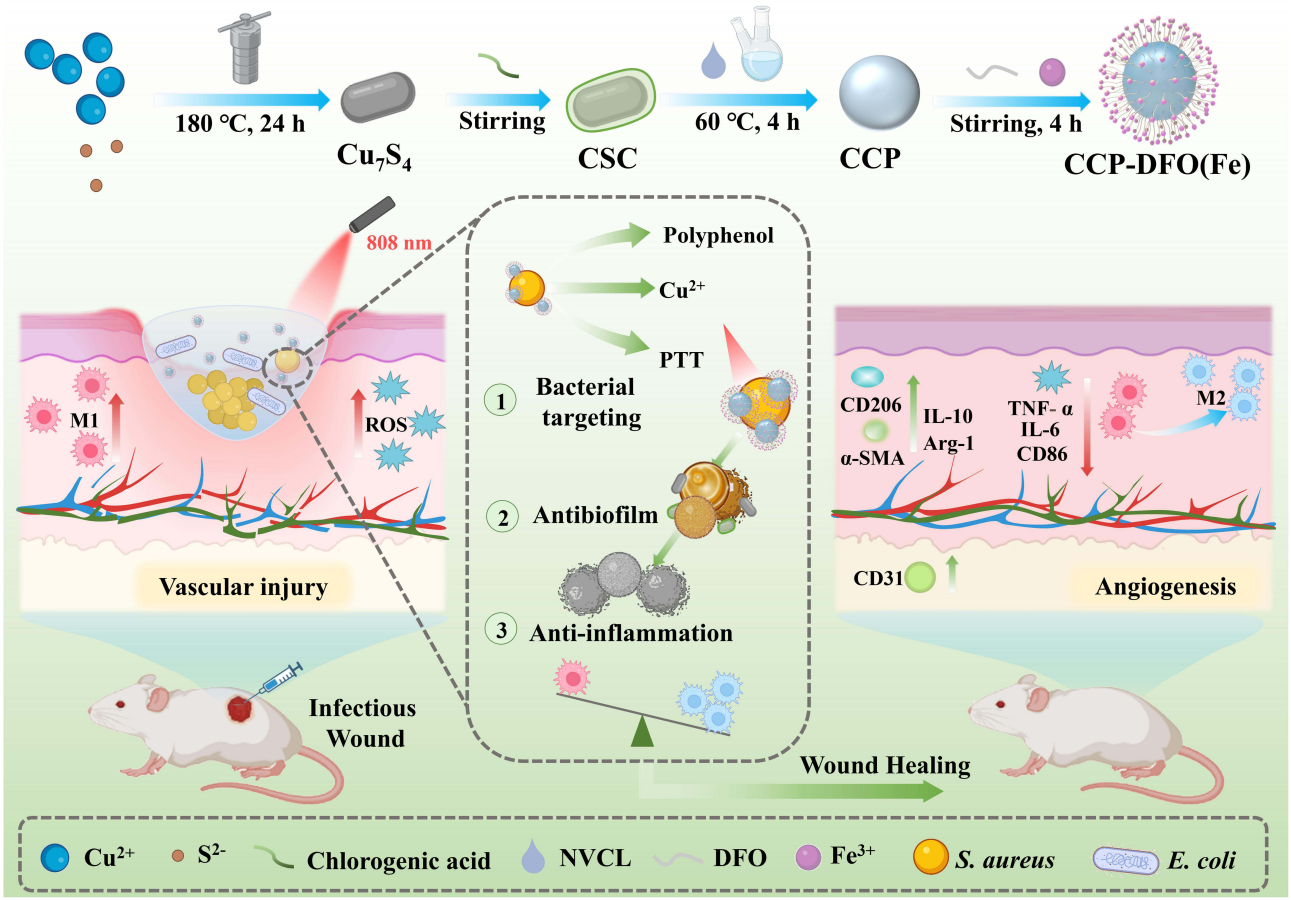

Figure 1 Schematic illustration of the fabrication and working mechanism of the CCP-DFO(Fe) nanoplatform for infected wound therapy.

Synthesis of CCP-DFO(Fe) Nanoparticle

0.3 g of cupric acetate anhydrous was added to 40 mL of DMAc. Under stirring, 0.4 g of PVP and 200 μL of aniline were introduced and dissolved by stirring for 30 minutes. Then, 0.15 g of thiourea was added, and stirring was continued until complete dissolution. The resulting suspension was transferred into a high-temperature hydrothermal autoclave equipped with a polytetrafluoroethylene liner and reacted at 150 °C for 20 hours. The product was isolated by centrifugation (4 °C, 10,000 rpm, 5 min) following cooling, washed alternately three times each with deionized water and ethanol, and finally freeze-dried to obtain Cu_7S_4 NPs.

Cu_7S_4@CGA (CSC) was synthesized by mixing 5 mL of a 1 mg/mL Cu_7S_4 solution with 5 mL of a 2 mg/mL CGA solution under stirring at pH 7.4 for 4 hours. The precipitate was then collected by centrifugation (4 °C, 10,000 rpm, 5 min), washed three times with water, and subsequently isolated. A UV standard curve for CGA was established at concentrations of 0, 1.25, 2.5, 5, 10, 20, and 25 μg/mL. The encapsulation efficiency (EE%) and drug loading content (DLC%) of CGA were determined by analyzing the supernatant liquid using ultraviolet-visible (UV-Vis) spectroscopy at 324 nm.

To enhance the stability and incorporate targeting capability of the nanoparticles, they were encapsulated with PVCL. The monomers were directly added as part of the reaction medium. Specifically, 88 mg of NVCL, 8 mg of OEGMA, 2 mg of AA, and 0.6 mg of MBA were weighed and added to an aqueous suspension containing 1 mg/mL CSC NPs. The mixture was stirred magnetically until homogeneous. It was then slowly purged with nitrogen for 20 minutes to remove oxygen, followed by the addition of 1.0 mg of VA-044 under continued nitrogen protection. The reaction was allowed to proceed at 60 °C in a constant-temperature bath for 4 hours. The reaction mixture was then cooled to room temperature. The resulting nanoparticles were collected by centrifugation to remove unreacted polymers and residual monomers (4 °C, 8000 rpm, 5 min), washed consecutively 3 times, and finally redispersed in PBS (pH 7.4) to obtain the CCP NPs.

Synthesis of CCP-DFO(Fe) NPs: CCP NPs were redispersed in MES buffer (0.1 M, pH 5.5, 10 mL) and activated by the addition of EDC (10 mg) and NHS (15 mg). Subsequently, the particles were collected by centrifugation at 8000 rpm for 5 min, washed with water, and redispersed in PBS (pH 7.4). A solution of DFO (2 mL, 10 mM) was then added to the activated particle suspension, and the mixture was gently shaken at room temperature for 2 h. After the coupling reaction, unbound DFO was removed by dialysis to afford CCP-DFO NPs. The CCP-DFO NPs were suspended in PBS buffer (pH 6.0–7.0). A 3 mM $FeCl_3$ solution was added dropwise at a molar ratio of Fe^{3+}: DFO = 1.2:1, followed by incubation with agitation at 600 rpm for 30 min. Excess Fe^{3+} ions were removed by centrifugation and washing (4 °C, 8000 rpm, 5 min). The final product, designated as CCP-DFO(Fe) NPs, was obtained. To evaluate the storage stability of the nanoparticles, CCP-DFO(Fe) was dispersed in different media, including pH 6.5, pH 7.4, pH 8.5, and serum, and stored under ambient conditions. The dispersion state of the nanoparticles was visually monitored over a period of 7 days.

Characterization of CCP-DFO(Fe) Nanoparticle

A series of characterization techniques were employed to analyze the synthesized materials. Morphology was examined using transmission electron microscopy (TEM; JEM-F200, JEOL, Japan) and scanning electron microscopy (SEM, Sigma 360, ZEISS, Germany), and surface charge was determined via a Zetasizer Pro analyzer (Malvern Panalytical, UK). For spectral analysis, a Nicolet iS5 spectrometer (Thermo Fisher Scientific, USA) was used to acquire both UV-Vis absorption and FTIR spectra. The crystalline structure was investigated by X-ray powder diffraction (XRD; D8 ADVANCE, Bruker, Germany), and the surface chemistry was probed via X-ray photoelectron spectroscopy (XPS) on a Thermo Fisher Scientific Nexsa system.

Assessment of Photothermal Performance and Release Behavior

For the quantitative assessment of the photothermal conversion capacity of the materials, CCP-DFO(Fe) and other nanoparticles were dispersed in aqueous solutions and exposed to an 808 nm NIR laser. Throughout the irradiation period, the temperature fluctuation and spatial thermal distribution features of the solutions were collected and documented in real time via an infrared thermal imaging camera. Utilizing the measured heating and natural cooling profiles, the photothermal conversion efficiency of the materials was determined; moreover, their photothermal stability was assessed through repeated laser on-off cycling tests.

Based on the in vitro photothermal heating characteristics of the nanoparticles, CCP-DFO(Fe) nanoparticles (2 mg/mL) dispersed in PBS (pH 7.4) were irradiated at a NIR power density of 0.5 $W \cdot cm^{-2}$. After 4 min of irradiation, the temperature rose to 44.3 °C. Subsequently, the temperature was maintained within the range of 40–45 °C by alternately turning off the NIR for 1 min and then re-irradiating for 2 min. The total testing duration was 10 min, during which the supernatant was collected every minute for subsequent release measurements. The cumulative release of CGA in the supernatant was quantified by UV-Vis spectroscopy at 323 nm based on its characteristic absorbance.

Evaluation of Antibacterial, Anti-Biofilm, and Antioxidant Properties

The antibacterial properties of the nanoplatform were examined employing *S aureus* and *Escherichia. coli (E. coli)* as model microorganisms representing Gram-positive and Gram-negative species. To explore the contribution of photothermal activation, designated samples were exposed to near-infrared light (808 nm) at an irradiation power of 0.5 $W \cdot cm^{-2}$ for a duration of 10 min. Bacterial suspensions prepared in LB medium (1×10^6 $CFU \cdot mL^{-1}$) were mixed at a 1:1 volume ratio with PBS or various material formulations, including Cu_7S_4, Cu_7S_4@CGA, CCP, and CCP-DFO(Fe), with CCP-DFO(Fe) receiving simultaneous NIR irradiation. Antibacterial efficacy was quantified by monitoring changes in bacterial turbidity at 600 nm at 0, 2, 4, 6, and 8 h during the incubation period. After 8 h of exposure, antibacterial efficacy was quantified by diluting bacterial suspensions stepwise in PBS and spreading 100 μL portions onto nutrient agar plates, followed by incubation for CFU enumeration. Following antibacterial treatment, bacterial cells were collected and fixed with 2.5% glutaraldehyde at 4 °C overnight. The samples were then dehydrated through a graded ethanol series (30%, 50%, 70%, 90%, and 100%), air-dried, and sputter-coated with gold. Morphological changes were observed using SEM.

Bacterial biofilms were cultured in sterile 24-well plates by incubating 800 μL of bacteria (revived in broth containing 1% glucose) with 200 μL of nanoparticle PBS solution (1 mg/mL) for 36 hours in a biochemical incubator. After incubation, the culture medium was carefully removed. Each well was gently washed with 500 μL of PBS (pH 7.4) to remove non-adherent planktonic bacteria. For fixation and staining, 500 μL of methanol was added to each well and allowed to stand at room temperature for 15 minutes. After washing and air-drying, 200 μL of 0.1% (w/v) crystal violet solution was added and allowed to stain for 30 minutes at room temperature. Following another wash and drying step, the plates were photographed. To quantify biofilm biomass, 200 μL of 95% ethanol was added to each well and incubated for 15 minutes with gentle shaking to elute the crystal violet bound to the biofilm. The optical density (OD) of the eluted solution was then measured at 570 nm using a microplate reader.

The free radical quenching ability of the prepared samples was assessed using commercially available DPPH, ABTS, and MB assays. For each test, the radical working solution (900 μL) was combined with anhydrous ethanol (900 μL) and nanoparticle dispersions (200 μL) from the respective groups. Temporal changes in absorbance were continuously monitored by UV-Vis spectroscopy to generate reaction profiles. The corresponding scavenging efficiencies toward DPPH, ABTS, and MB radicals were determined according to Eq. (1):

$$\text{Radical scavening ratio} = 1 - \frac{A_T - A_P}{A_N - A_P} \times 100\% \quad (1)$$

where A_N, A_P, and A_T denote the absorbance values of the negative control, positive control, and tested sample, respectively.

The hydroxyl radical (•OH) scavenging ability was evaluated via a salicylic acid chromogenic assay. A mixture of 200 μL of 10 mM $FeSO_4$ and 100 μL of 10 mM H_2O_2 was allowed to react for 5 min, followed by the addition of 100 μL of 18 mM salicylic acid for color development. Subsequently, 200 μL of nanoparticle aqueous dispersion (1 mg/mL) and 400 μL of deionized water were added. After incubation for 15 min, the supernatant was collected by centrifugation and its absorbance was measured by UV-Vis spectroscopy.

Biocompatibility Evaluation

The biocompatibility of the materials was evaluated using human umbilical vein endothelial cells (HUVECs, purchased from Wuhan Shangen Biotechnology Co., Ltd). Cells were cultured for 24 and 48 hours with PBS (Control), CSC, CCP-DFO(Fe), or CCP-DFO(Fe)+NIR groups irradiation. Cell viability and proliferation were assessed via live/dead staining and the CCK-8 assay. To observe morphological changes, HUVECs were incubated with material extracts for 3 days. Following specific staining of the cytoskeleton, cellular morphology was examined using confocal fluorescence microscopy.

To evaluate the cytocompatibility under different photothermal conditions, HUVECs were incubated with the CCP-DFO(Fe) nanoplatform and exposed to NIR irradiation at varying power densities (0, 0.4, 0.45, 0.5, 0.55, 0.6 and 0.7 $W \cdot cm^{-2}$) for 10 minutes. After irradiation, cells were cultured for 24 hours, then cell viability was assessed using a standard CCK-8 assay. The corresponding temperature changes under each irradiation condition were simultaneously recorded using an infrared thermal imaging system.

Intracellular ROS Elimination Assay

The cellular antioxidative performance of the materials was evaluated in HUVECs. Cells were exposed to material-derived extracts for 24 h and subsequently challenged with hydrogen peroxide (H_2O_2, 100 μM). Cell survival was assessed by combining live/dead fluorescence staining with CCK-8 analysis, whereas intracellular ROS production was evaluated using DCFH-DA-based fluorescence detection.

In vitro Evaluation of Macrophage Polarization and Inflammatory Response

RAW264.7 macrophages (purchased from Wuhan Shangen Biotechnology Co., Ltd) subjected to inflammatory challenge were used to examine the immunoregulatory effects of the materials. Cells were first primed with LPS (100 ng mL^{-1}) for 24 h, followed by a second 24 h incubation with PBS, CSC, CCP-DFO(Fe), or CCP-DFO(Fe)+NIR nanoparticles. Macrophage phenotypes were identified by immunofluorescence staining using CD68 as a macrophage marker and

CD86/CD206 to distinguish M1- and M2-like states. Fluorescence images were acquired on a Nikon Eclipse Ti microscope and analyzed to determine phenotype distribution. Inflammatory cytokines released into the culture medium, including IL-1β, TNF-α, IL-10, and Arg-1, were quantified by ELISA.

Establishment and Treatment of a Bacteria-Infected Full-Thickness Wound Model

Male Sprague-Dawley rats (230–250 g) were used. All animal experiments complied with the ARRIVE guidelines and followed the ethical guidelines established by the National Research Council for laboratory animal use and were approved by the Animal Ethics Committee of the First Affiliated Hospital of University of South China (Approval No. 11000302–2). After one week of acclimation, the rats were anesthetized, and the hair on their dorsum was shaved. Two full-thickness circular wounds (approximately 10 mm in diameter) were created symmetrically on each side of the dorsal midline using a sterile biopsy punch. To establish an infected wound model, a bacterial suspension of Gram-positive Staphylococcus aureus (1×10^8 CFU·mL^{-1}, cultured in liquid medium at 37 °C for 18 h) was topically applied to the wound area. The wounds were then treated daily with PBS (Control), CSC, CCP-DFO(Fe), or CCP-DFO (Fe)+NIR group. For the photothermal treatment group, wounds were irradiated with an 808 nm laser at a power density of 0.5 W/cm^2 for 10 min per day. Wound closure was monitored by regular photography, and the healing rate was quantified using Image J software.

To evaluate the photothermal performance and practical feasibility of the nanoplatform in vivo, SD rat wound models were subjected to NIR irradiation (0.5 W·cm^{-2}), and the temperature changes at the wound site were monitored using an infrared thermal imaging system. The irradiation protocol consisted of an initial continuous exposure for 2 min, followed by intermittent irradiation with alternating 1 min on/off cycles for a total duration of 10 min. Temperature evolution and heating/cooling cycles were recorded to assess photothermal stability and controllability.

On day 14, rats were euthanized and wound tissues harvested. Bacteria from the wound surface were sampled using sterile swabs, serially diluted (up to 10^6-fold in PBS), plated on nutrient agar (100 μL aliquots), and incubated for colony-forming unit (CFU) counting to assess the bactericidal effect. The excised wound tissues and surrounding skin were subjected to histological evaluation, including hematoxylin and eosin (H&E) staining, Masson trichrome staining, myeloperoxidase (MPO) staining, immunofluorescence staining for CD86 and CD206 (macrophage polarization markers), and immunofluorescence for α-smooth muscle actin (α-SMA) and CD31 (vascular markers).

Statistical Analysis

All results are reported as mean values with corresponding standard deviations unless otherwise indicated. Experiments were independently repeated three times (n = 3). Statistical comparisons were performed using one-way ANOVA followed by Tukey's post hoc test, implemented with SPSS software (version 27.0, IBM, USA). Statistical significance was assigned at $p < 0.05$, $p < 0.01$, and $p < 0.001$. Symbols (*) and ($^{\#}$) denote differences versus the normal control and model group, respectively.

Results and Discussion

Fabrication and Characterization of CCP-DFO(Fe) Nanoplatform

The CCP-DFO(Fe) nanoparticles in this study were fabricated via a layer-by-layer assembly approach. Initially, Cu_7S_4 nanoparticles served as the core substrate. CGA was adsorbed onto their surface through electrostatic interaction. The particles were then encapsulated with a thermosensitive PVCL polymer layer. The amino groups of DFO were covalently conjugated to the carboxyl groups within the PVCL layer via an amide coupling reaction. Finally, the addition of Fe^{3+} ions led to their capture and chelation by DFO, resulting in the formation of the final CCP-DFO(Fe) nanoparticles. The as-synthesized Cu_7S_4 nanoparticles were first thoroughly characterized. XRD analysis revealed that the nanoparticles crystallized predominantly along the (102) plane, exhibiting a well-defined hexagonal phase (JCPDS No. 00-023-0958) (Figure 2A). The absence of impurity or additional phase peaks in the XRD pattern confirmed the high purity of the sample. The elemental composition and surface chemical states of the Cu_7S_4 sample were analyzed by XPS. The high-resolution XPS spectra (Figure 2B–D) displayed characteristic peaks for Cu $2p_{1/2}$ and Cu $2p_{3/2}$ at binding energies of 951.5 eV and 931.5 eV, respectively. Peaks corresponding

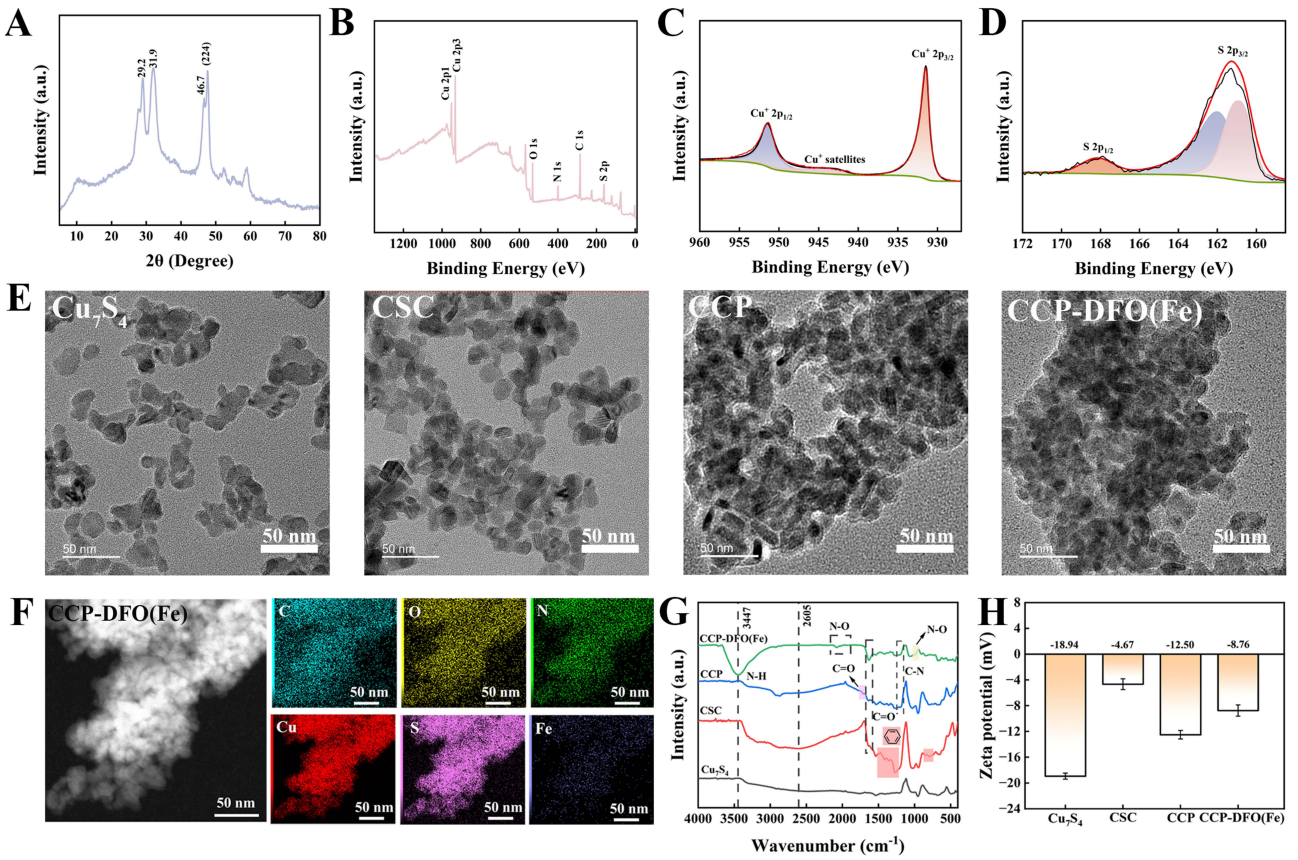

Figure 2 (**A**) XRD pattern of Cu_7S_4 nanoparticles. (**B–D**) XPS spectra of Cu_7S_4. (**E**) TEM images showing the morphologies of Cu_7S_4, CSC, CCP, and CCP-DFO(Fe). (**F**) Elemental mapping of CCP-DFO(Fe) nanoparticles. (**G**) FT-IR spectrum of Cu_7S_4, CGA, CCP, and CCP-DFO(Fe) NPs. (**H**) Zeta potential measurements.

to S $2p_{1/2}$ and S $2p_{3/2}$ were observed at 162.1 eV and 161.3 eV, respectively. XPS analysis indicated that copper exists predominantly in the +1 oxidation state (Cu^+), while sulfur is present primarily as S^{2-}. These results are consistent with the chemical structure of Cu_7S_4, confirming the high purity of the synthesized sample. TEM images (Figure 2E) revealed a gradual increase in particle size during the formation process. Specifically, the CCP particles exhibited an apparent organic membrane-like layer on their surface due to the encapsulation of the PVCL shell, which rendered the particle contours less distinct. With the continuous adsorption and coating of the outer components, the particles underwent gradual growth accompanied by a certain degree of aggregation. The average particle sizes of Cu_7S_4, CSC, CCP, and CCP-DFO(Fe) were approximately 18.0 ± 0.3 nm, 20.5 ± 2.0 nm, 22.1 ± 3.2 nm, and 24.5 ± 0.4 nm, respectively (Figure S1A–D). Elemental mapping confirmed the presence and uniform distribution of copper and sulfur on the nanoparticle surface. Owing to the presence of CGA, PVCL, and DFO(Fe) in the outer layers, distinct enrichment of carbon, oxygen, and nitrogen was observed on the particle surface (Figures 2F and S2A–D). A clear signal of iron in the outer layer further verified the successful loading of DFO(Fe).

In the FT-IR spectra (Figure 2G), the absorption peak at 1430 cm^{-1} corresponds to the skeletal vibration of the aromatic ring in CGA, while the peak at 790 cm^{-1} is attributed to the out-of-plane bending of aromatic C-H bonds. The broad absorption in the 1750–3400 cm^{-1} region suggests possible hydrogen bonding and other non-covalent interactions between CSC and the Cu_7S_4 surface. Furthermore, the spectrum of CCP nanoparticles exhibits a characteristic C=O stretching vibration at 1720 cm^{-1}, originating from the carbonyl group of the amide moiety in the caprolactam ring of the polymer side chain, and a C-N absorption at 1200 cm^{-1}, both verifying the successful encapsulation by PVCL. Subsequently, in the spectrum of CCP-DFO(Fe) particles, a sharp peak at 3347 cm^{-1} can be ascribed to the presence of O-H/N-H groups in the DFO backbone, and the absorption at 987 cm^{-1} represents the N-O stretching vibration in the iron-hydroxamate structure, further confirming the formation of a stable Fe-DFO chelate. Furthermore, the successful

loading of CGA and DFO(Fe) was confirmed by UV-Vis spectroscopic analysis of the nanoparticle supernatant, in which the characteristic absorption peaks of CGA and DFO(Fe) were observed at 324 nm and 425 nm, respectively. Using a UV absorbance standard curve, the drug loading content of CGA was calculated to be 23.75%, and the grafting rate of DFO(Fe) was determined to be 34.58% (Figures S3A, B and S4A, B). The mass percentages of the components (Cu_7S_4, CGA, PVCL, and DFO(Fe)) were obtained by a difference method as 70.3%, 14.93%, 8.26%, and 6.50%, respectively (Table S1). Zeta potential measurements (Figure 2H) revealed variations in surface charge following sequential modifications, with the final CCP-DFO(Fe) nanoparticles exhibiting a zeta potential of −8.76 ± 0.87 mV. In addition, as revealed by the particle storage stability experiments, no visible aggregation or precipitation was observed in any of the tested media over 7 days, indicating that the nanoparticles maintained good dispersion stability under different pH conditions and in serum. These results demonstrate satisfactory short-term storage stability and suggest that the CCP-DFO(Fe) system is suitable for potential biomedical applications (Figure S5).

The Photothermal, Release Properties and Antioxidant Activity of CCP-DFO(Fe) Nanoparticles

Copper sulfide-based nanomaterials, including Cu_7S_4, are recognized for their strong near-infrared absorption and efficient photothermal conversion.[40] As shown in Figures 3A and S6A, the photothermal effects of Cu_7S_4, CSC, CCP, and CCP-DFO(Fe) nanoparticles were significantly stronger than that of deionized water. Even with the outer-layer adsorption and encapsulation of organic molecules, the temperature of each group rose to approximately 42 °C within 4 minutes, confirming that Cu_7S_4 nanoparticles are the primary contributor to the photothermal effect and that the outer layers do not interfere with its performance. Under a laser power density of 0.5 W/cm^2, CCP-DFO(Fe) reached 43.1 °C

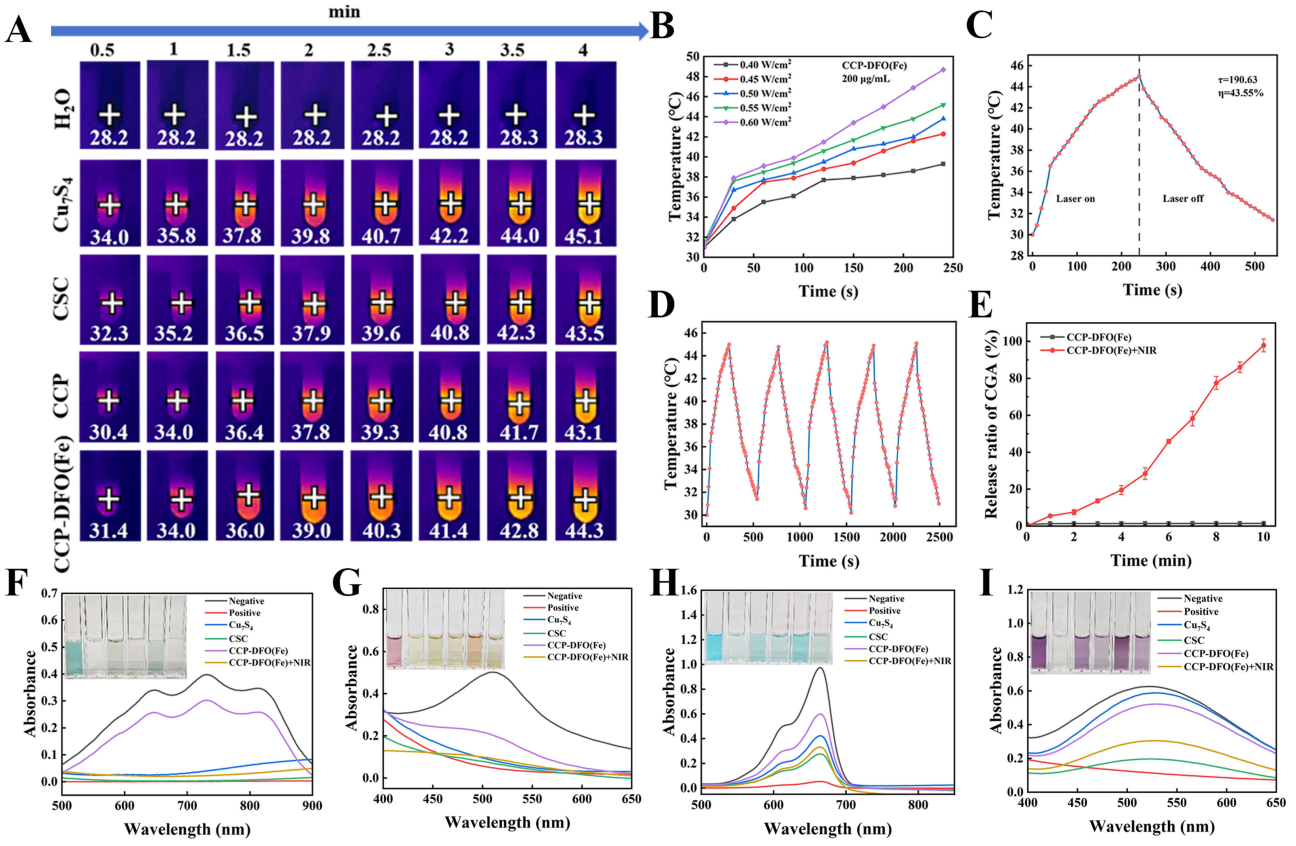

Figure 3 (**A**) Infrared thermal images of various nanoparticles under NIR irradiation at 0.50 W/cm^2. (**B**) Temperature evolution of CCP-DFO(Fe) under varying irradiation durations and power densities. (**C**) Thermal profile of CCP-DFO(Fe) during NIR ON/OFF cycles at 0.50 W/cm^2. (**D**) Temperature response of CCP-DFO(Fe) over repeated ON/OFF cycles at 0.50 W/cm^2. (**E**) Cumulative CGA release from CCP-DFO(Fe) nanoparticles under NIR ON/OFF irradiation at 0.50 W/cm^2. (**F-I**) Radical scavenging activities (ABTS, DPPH, MB, •OH) were evaluated using UV-Vis spectroscopy with representative photographs.

https://doi.org/10.2147/IJN.S594688

within 4 minutes (Figure 3B). Increasing the concentration of CCP-DFO(Fe) resulted in a corresponding rise in temperature (Figure S6B). Under a laser intensity of 0.50 W/cm^2 and a particle concentration of 200 μg/mL, CCP-DFO(Fe) reached 42 °C within 4 minutes, remaining within the safe range for photothermal therapy (42–45 °C).[46] The nanoparticles exhibited a trend of rapid heating and gradual cooling (Figures 3C and S6C), with a photothermal conversion efficiency of 43.55%, indicating that the material ensures both heating efficiency and treatment safety. Furthermore, as shown in Figure 3D, the CCP-DFO(Fe) nanoparticles maintained their characteristics after five heating and cooling cycles, demonstrating excellent photothermal stability. These results indicate that CCP-DFO(Fe) effectively transforms 808 nm laser energy into heat, demonstrating efficient photothermal conversion.

Owing to the encapsulation by the thermosensitive PVCL layer, controlled release from the particles can be achieved via photothermal stimulation. Upon NIR irradiation, the phase transition of PVCL is triggered, exposing the encapsulated CGA. The release profile was evaluated by measuring the CGA content in the supernatant. As shown in Figure 3E, compared with the non-photothermal group, a temperature range of 40–45 °C was maintained in the photothermal group between 4 min and 10 min. Under these conditions, a gradual increase in the cumulative release rate of CGA was observed, and a release rate of 97.87 ± 3.49% was reached at the 10 min time point.

In bacterially infected wounds, prolonged and excessive ROS exacerbate local oxidative stress, leading to lipid peroxidation, protein dysfunction, and DNA damage, which collectively impede cell migration and proliferation and delay tissue repair.[47] The ABTS assay (Figures 3F and S7A) showed that Cu_7S_4 and CSC nanoparticles efficiently scavenged radicals (86.42 ± 1.68% and 97.13 ± 2.17%, respectively), whereas CCP-DFO(Fe) exhibited lower activity (23.99 ± 2.84%) due to the PVCL layer acting as a physical barrier. Upon NIR irradiation, the PVCL phase transition released CGA and Cu_7S_4, restoring the DPPH scavenging efficiency of CCP-DFO(Fe)+NIR to 91.28 ± 1.08%. Similar enhancements were observed in DPPH and MB assays (Figures 3G, H and S7B, C), with CCP-DFO(Fe)+NIR consistently exceeding 90% scavenging.

Additionally, the •OH scavenging ability was evaluated using a salicylic acid chromogenic assay. The •OH generated via the Fenton reaction specifically react with salicylic acid to form a purplish-red iron complex of 2,3-dihydroxybenzoic acid, which exhibits characteristic absorption at 510 nm. The decrease in absorbance after adding the nanoparticles quantitatively reflects their •OH scavenging efficiency. Except for Cu_7S_4, which showed no significant •OH scavenging effect, the results from the other particles were consistent with the aforementioned radical scavenging experiments (Figures 3I and S7D), with the CCP-DFO(Fe)+NIR group exhibiting an OD value of 0.299 ± 0.039. In summary, the CCP-DFO(Fe) nanoplatform integrates precise photothermal regulation, stimulus-responsive drug release, and potent radical scavenging capabilities, demonstrating considerable potential for the treatment of infected wounds.

Antibacterial Performance of Nanoparticles

Effective suppression of pathogenic microorganisms is essential to initiate tissue regeneration in infected wounds. Given the inherent antibacterial activity of CGA and the partial bactericidal effect of copper-based materials via ion release, the in vitro antibacterial performance of CCP-DFO(Fe) was systematically evaluated using *S. aureus* and *E. coli* as model strains. Bacterial growth curves (Figure 4A and B) demonstrated that Cu_7S_4 and CSC markedly suppressed bacterial proliferation after 6 h, with OD values substantially lower than the PBS control. The CCP group exhibited a slightly higher OD value than CSC group, likely due to the shielding effect of the thermosensitive polymer layer. Compared with the CCP-DFO group, the CCP-DFO(Fe) group demonstrated a more rapid decline in OD value at 6 h, attributable to the bacterial targeting of DFO(Fe). Upon NIR irradiation, the CCP-DFO(Fe)+NIR group showed a further decrease in OD compared to CCP-DFO(Fe), indicating enhanced antibacterial efficacy under photothermal stimulation. This effect is attributed to the combined action of released CGA and local hyperthermia generated by Cu_7S_4. Plate colony counts and bacterial survival data (Figures 4C and S8) aligned with the trends observed in the growth curves, confirming the potent and NIR-enhanced antibacterial activity of CCP-DFO(Fe).

Chronic wound infections often persist due to the inability of antibiotics to eradicate biofilms. Bacterial biofilms consist of extracellular polymeric substances (EPS) that form a dense physical barrier, limiting drug penetration into the deeper microbial community. In this study, the ability of CCP-DFO(Fe) to disrupt biofilm maturation was evaluated. Crystal violet staining of bacterial biofilms revealed that the $FeCl_3$ group showed no significant anti-biofilm effect, indicating that Fe^{3+} ions alone lack antibacterial activity. Treatment with Cu_7S_4 and CSC markedly reduced biofilm formation, while the biofilm integrity remained higher in the CCP group due to the shielding effect of the PVCL layer (Figure 4D). In contrast, biofilm

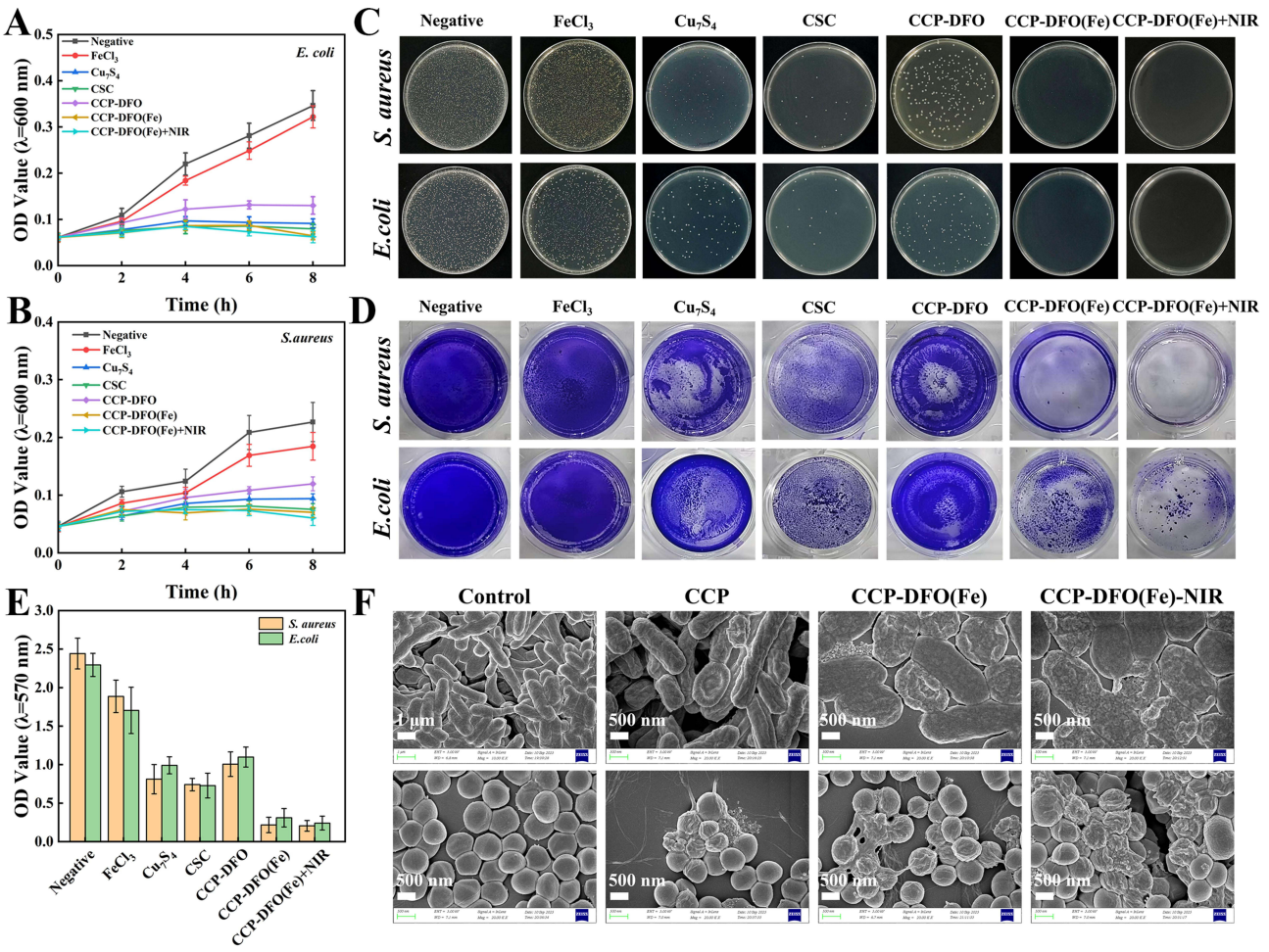

Figure 4 (**A** and **B**) Growth profiles of *E. coli* and *S. aureus* following exposure to different materials. (**C**) Representative colony images after 6 h incubation. (**D**) Crystal violet staining of mature biofilms following treatment. (**E**) OD_{570} values of dissolved crystal violet (n = 3). (**F**) SEM images showing bacterial morphology after treatment.

disruption was pronounced in the CCP-DFO(Fe) group, and the CCP-DFO(Fe)+NIR group exhibited the strongest inhibition, with almost no visible biofilm remaining. These observations align with the earlier plate-counting results. Quantitative biofilm OD measurements further confirmed the above trends (Figure 4E). Together, these findings demonstrate that NIR irradiation initiates a cascade of synergistic effects within the CCP-DFO(Fe) nanoplatform: the photothermal action of Cu_7S_4 not only directly damages biofilms but also triggers the release of CGA and Cu^{2+}, which collectively enhance the potent biofilm-disrupting activity.

SEM was employed to examine morphological alterations in bacterial cells. Compared to intact bacteria in the PBS control group, *E. coli* treated with CCP exhibited noticeable surface shrinkage and invagination, while *S. aureus* cells displayed more severe damage, including pore formation and rupture (Figure 4F). These changes reflect the combined antibacterial effects of CGA and copper ions. CGA disrupts membrane integrity by interacting with lipid bilayers, and copper ions further compromise membrane structure through direct binding to phospholipids and membrane proteins, leading to increased permeability and structural collapse. After treatment with the CCP-DFO(Fe) group, bacterial membranes showed more extensive pores and wrinkling, with some cells appearing deformed, ruptured, and leaking intracellular contents. This effect can be attributed to DFO(Fe), which enhances membrane vulnerability through targeted iron competition and weakened bacterial metabolism. Such multimodal action resulted in severe structural damage and cytoplasmic leakage. Under NIR irradiation, the CCP-DFO(Fe)+NIR group induced widespread bacterial collapse and rupture, accompanied by prominent leakage of cytoplasmic material. These extreme morphological alterations are due to the synergistic actions of photothermal heating, which causes immediate membrane rupture and protein denaturation, and

https://doi.org/10.2147/IJN.S594688

the enhanced release of CGA and Cu^{2+}. Together, these factors overwhelm bacterial repair mechanisms and lead to irreversible structural disintegration. These findings indicate that CCP-DFO(Fe) exerts antibacterial activity through sequential and synergistic mechanisms: initial membrane disruption by CGA and Cu^{2+}, enhanced targeting and metabolic interference via DFO(Fe), and photothermally driven irreversible collapse.

Biocompatibility of CPP-DFO(Fe) Nanoparticles

Ensuring excellent biocompatibility is a fundamental prerequisite in nanomaterials research.[48] The cytotoxicity of the nanoparticles was assessed in HUVECs, with live/dead staining indicating over 95% cell viability after 24 and 48 h of exposure. Compared to the CSC group, the CCP-DFO(Fe) group and CCP-DFO(Fe)+NIR group exhibited a significant proliferative trend (Figure 5A). CCK-8 assay results (Figure 5B) further confirmed the absence of significant cytotoxicity for all tested particles, with or without NIR irradiation, as cell viability remained above 90.0%. Additionally, cell viability remained at 99.84 ± 0.245% under 0.5 $W \cdot cm^{-2}$ irradiation, corresponding to approximately 44.2 °C, whereas it decreased to 70.31 ± 0.287% at a higher power density of 0.7 $W \cdot cm^{-2}$, corresponding to approximately 51.2 °C, indicating that elevated temperatures induce thermal cytotoxicity (Figure S9). These results support the safety of the selected mild photothermal condition. Cytoskeleton staining revealed clear and continuous F-actin fibers in all groups, with intact cell morphology and well-spread morphology, and no observable contraction or cytoskeletal disruption (Figure 5C). Notably, even in the CSC and CCP-DFO(Fe)+NIR groups, the cytoskeleton maintained its normal architecture, indicating that neither the material itself nor the photothermal effect under NIR excitation caused obvious cytoskeletal damage, thus preliminarily confirming good biocompatibility. Quantitative analysis further indicated that CSC treatment resulted in a slight reduction in cell spreading area, whereas cells treated with CCP-DFO(Fe) and CCP-DFO(Fe)+NIR showed a recovering trend (Figure 5D). This phenomenon may be attributed to the encapsulation by the thermosensitive layer, which moderates the release of active components, thereby reducing their potential impact on the cells.

Ameliorating Oxidative Stress, Promoting Cell Migration, and Stimulating Angiogenesis by CPP-DFO(Fe) Nanoparticles in vitro

To simulate the sustained inflammatory activation in the wound microenvironment, an oxidative stress model was established by treating cells with H_2O_2, thereby further evaluating the ROS-scavenging and antioxidative activity of the nanoparticles in vitro. Live/dead staining (Figure 5E) showed extensive cell death in H_2O_2-treated HUVECs, while treatment with any of the nanoparticles reduced apoptosis. Remarkably, CCP-DFO(Fe)+NIR restored cell survival to levels similar to the untreated control, indicating effective mitigation of H_2O_2-induced oxidative damage. Consistently, CCK-8 assays (Figure 5F) confirmed that CCP-DFO(Fe)+NIR preserved superior cell viability under oxidative conditions relative to the other groups.

Wound healing is a highly coordinated biological process involving the synergistic actions of various skin cells, growth factors, and physiological events.[49] Fibroblast migration and collagen secretion are critical for granulation tissue formation, while endothelial cells mediate angiogenesis.[50] Therefore, the pro-angiogenic and wound-healing potential of CCP-DFO(Fe) nanoparticles was evaluated in vitro. First, a scratch wound assay was performed to simulate cell migration. After 12 h of treatment, HUVEC migration was observed under an optical microscope. The CCP-DFO(Fe)+NIR group exhibited a significantly higher migration rate (61.04 ± 0.61%) compared to the H_2O_2-induced model group (37.13 ± 0.37%) (Figure 5G and H). Crystal violet staining further confirmed that nanoparticle treatment markedly reversed the H_2O_2-induced inhibition of cell migration (Figure 5I and J), demonstrating the material's ability to counteract oxidative stress-impaired migratory function. Subsequently, angiogenesis was assessed using a Matrigel-based tube formation assay, with the tubular networks formed by HUVECs stained with calcein. Compared to the PBS group, all material-treated groups maintained relatively intact tubular networks (Figure 5K). Quantitative analysis corroborated that the CSC, CCP-DFO(Fe), and CCP-DFO(Fe)+NIR groups showed increased branch points and greater average tube length relative to the model group (Figure 5L).

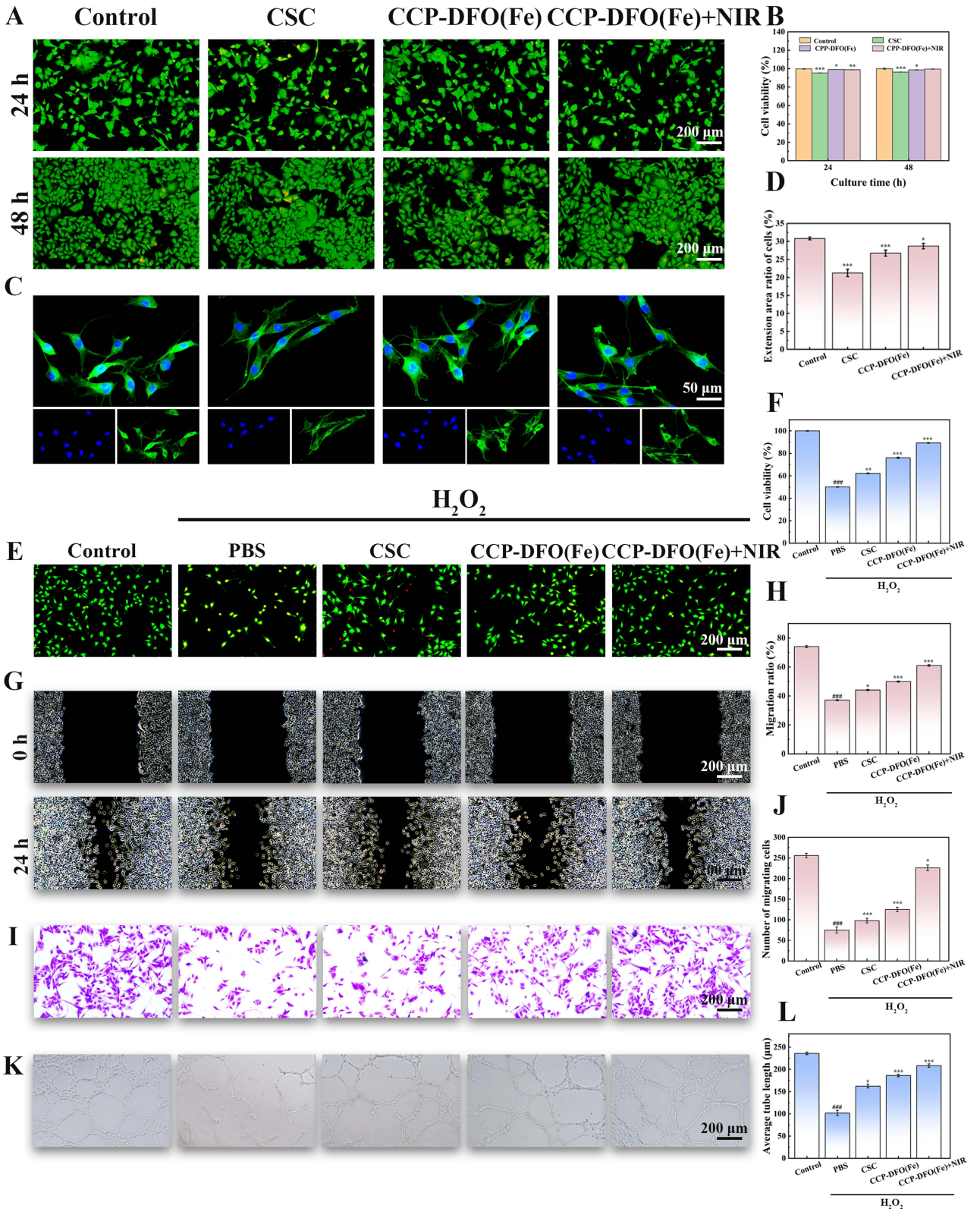

Figure 5 (**A**) Live/dead staining and (**B**) quantification of HUVEC viability after 24 and 48 h exposure to various materials. (**C**) Cytoskeleton morphology and (**D**) extension area ratio of HUVECs after material treatment. Under oxidative stress induced by H_2O_2 co-treatment for 24 h, (**E**) live/dead staining and (**F**) cell viability were evaluated. (**G**) Fluorescence images and (**H**) quantitative analysis of cell migration were performed, along with (**I**) crystal violet staining and (**J**) migrated cell counts. (**K**) Tube formation capability and (**L**) average tube length were further assessed after H_2O_2 and material co-treatment. (Symbols (*) and ($^{\#}$) denote differences versus the normal control and model group, respectively. *p<0.05, **p<0.01, and ***p<0.001; $^{\#\#\#}p$<0.001).

https://doi.org/10.2147/IJN.S594688

Anti-Inflammatory and Antioxidant Activities of CPP-DFO(Fe) in vitro

To evaluate the intracellular antioxidant activity of the materials, the fluorescent probe DCFH-DA was used to detect changes in intracellular ROS levels. As shown in Figure 6A, after H_2O_2 stimulation, cells in the PBS group exhibited intense green fluorescence, indicating a sharp increase in intracellular ROS. All nanoparticle-treated groups exhibited markedly lower total intracellular ROS compared with the PBS control. Following treatment with CCP-DFO(Fe)+NIR, the fluorescence intensity was markedly diminished and comparable to that of the untreated Control group. These results

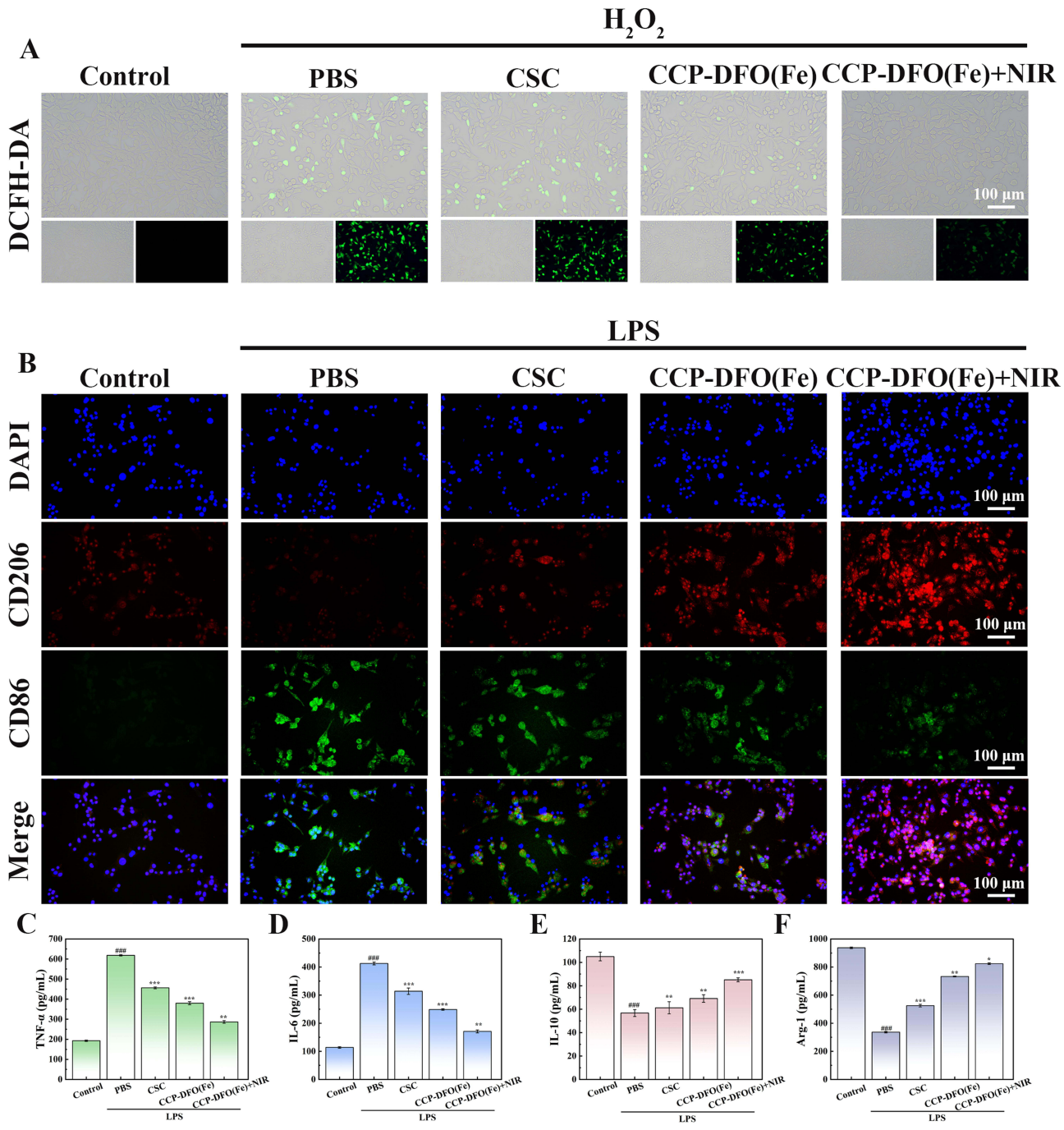

Figure 6 (**A**) DCFH-DA staining showing intracellular ROS in HUVECs after 24 h co-exposure to H_2O_2 and nanoparticles. (**B**) Immunofluorescence of CD86 (green, M1) and CD206 (red, M2) in RAW264.7 macrophages following nanoparticle treatment. Relative cytokine expression after 24 h co-culture with LPS and nanoparticles: (**C**) TNF-α, (**D**) IL-6, (**E**) IL-10, and (**F**) Arg-1. (Symbols (*) and ($^{\#}$) denote differences versus the normal control and model group, respectively. *p<0.05, **p<0.01, and ***p<0.001; $^{\#\#\#}p$<0.001).

https://doi.org/10.2147/IJN.S594688

clearly demonstrate that CCP-DFO(Fe) nanoparticles can effectively scavenge excess ROS induced by H_2O_2, exhibiting excellent intracellular antioxidant performance.

M2 polarization of macrophages is essential for resolving inflammation and supporting tissue repair in infected wounds.[51] In LPS-stimulated RAW264.7 cells (M1 model), the effects of nanoparticles on phenotype were assessed via CD86 (M1) and CD206 (M2) immunofluorescence. Displayed in Figure 6B, LPS (PBS group) strongly induced CD86 expression, whereas nanoparticle treatment progressively increased CD206 levels. CCP-DFO(Fe)+NIR produced the highest CD206 and lowest CD86 signals, indicating effective M2 polarization. Consistent with these observations, ELISA measurements (Figure 6C–F) revealed that nanoparticles reduced pro-inflammatory cytokines (IL-1β, TNF-α) and increased anti-inflammatory factors (IL-10, Arg-1) in a graded manner. The CCP-DFO(Fe)+NIR group showed the most pronounced anti-inflammatory effect, with pro-inflammatory cytokine levels approaching those of unstimulated controls. These results demonstrate that CCP-DFO(Fe), particularly under NIR irradiation, efficiently reprograms macrophages toward a pro-repair phenotype. These results demonstrate that CCP-DFO(Fe), particularly under NIR irradiation, efficiently reprograms macrophages toward a pro-repair phenotype. This effect may also be partially associated with the immunomodulatory activity of CGA, which has been reported to involve multiple macrophage-regulating pathways, including NF-κB-, JAK/STAT-, and Nrf2-related signaling, with Nrf2-mediated antioxidant regulation being particularly linked to M2 polarization.[33,35,36]

Observation of the Therapeutic Effect of CCP-DFO(Fe) on Bacterial Infected Wounds in vivo

A full-thickness skin wound model infected with both *E. coli* and *S. aureus* was established in SD rats to assess the in vivo antibacterial and wound-healing effects of the nanoparticles. As shown in Figure 7A, wound healing was monitored on days 0, 3, 7, 11, and 14. The control group exhibited slow healing, with substantial unhealed areas and visible scarring still present on day 11. In contrast, all nanoparticle-treated groups showed significantly improved wound closure rates (Figure 7B). Compared to the CSC group, the CCP-DFO(Fe) group displayed accelerated healing from day 3 onward, achieving a wound closure ratio of 94.99 ± 0.66% by day 14. The CCP-DFO(Fe)+NIR group exhibited the most pronounced repair outcome, with nearly complete wound closure, minimal scarring, and a healing ratio of 98.56 ± 1.08% on day 14. The in vivo antibacterial effect was further assessed. On day 14, infected skin samples from each group were collected, cultured for 24 h, and subjected to bacterial counting. As shown in Figure 7C and D, nanoparticle treatment significantly reduced bacterial loads compared to the control. The CCP-DFO(Fe) group showed stronger bactericidal activity than the CSC group, indicating the beneficial role of bacterial targeting by DFO(Fe). Notably, in the CCP-DFO(Fe)+NIR group, bacterial survival was nearly eliminated, which can be attributed to the combined effects of NIR-triggered CGA release and DFO(Fe)-mediated bacterial targeting.

Infrared thermal imaging showed that the wound temperature rapidly increased to approximately 44.8 °C within 2 min under 0.5 $W \cdot cm^{-2}$ irradiation, indicating effective photothermal activation in vivo. During subsequent intermittent irradiation, the temperature was maintained within 39.5–45.4 °C, demonstrating stable thermal control within a mild photothermal range. In addition, repeated heating/cooling cycles exhibited consistent temperature profiles, confirming good photothermal stability and controllability of the system (Figure S10A–D). To further evaluate in vivo biosafety, histological analysis of major organs was conducted on day 14 post-treatment, and no obvious pathological abnormalities were observed, indicating favorable in vivo biocompatibility within the studied period (Figure S11).

Wound samples harvested on days 7 and 14 were processed for H&E staining, revealing histologically significant differences in tissue repair (Figures 7E and S12A). In the control group, the newly formed epithelium at the wound edge appeared abnormally thickened, with disordered basal cells and abundant inflammatory cell infiltration. The CSC nanoparticle group exhibited noticeable improvement, showing reduced epithelial hyperplasia and a smaller wound area. The CCP-DFO(Fe) group exhibited a more continuous epithelium with well-preserved epithelial and dermal structures, increased formation of granulation tissue, and reduced inflammatory infiltration. Upon photothermal treatment, the CCP-DFO(Fe)+NIR group demonstrated the most favorable outcome, achieving nearly complete and regular epithelial regeneration, mature dermal remodeling, substantial conversion of granulation tissue into dense connective tissue, and almost complete resolution of inflammation. Quantitative assessment of epidermal thickness (Figure 7F) indicated that the CCP-DFO(Fe)+NIR group recovered to 26.82 ± 3.77 μm by day 14. Masson's trichrome staining provided further insight into collagen deposition within the newly formed skin tissue

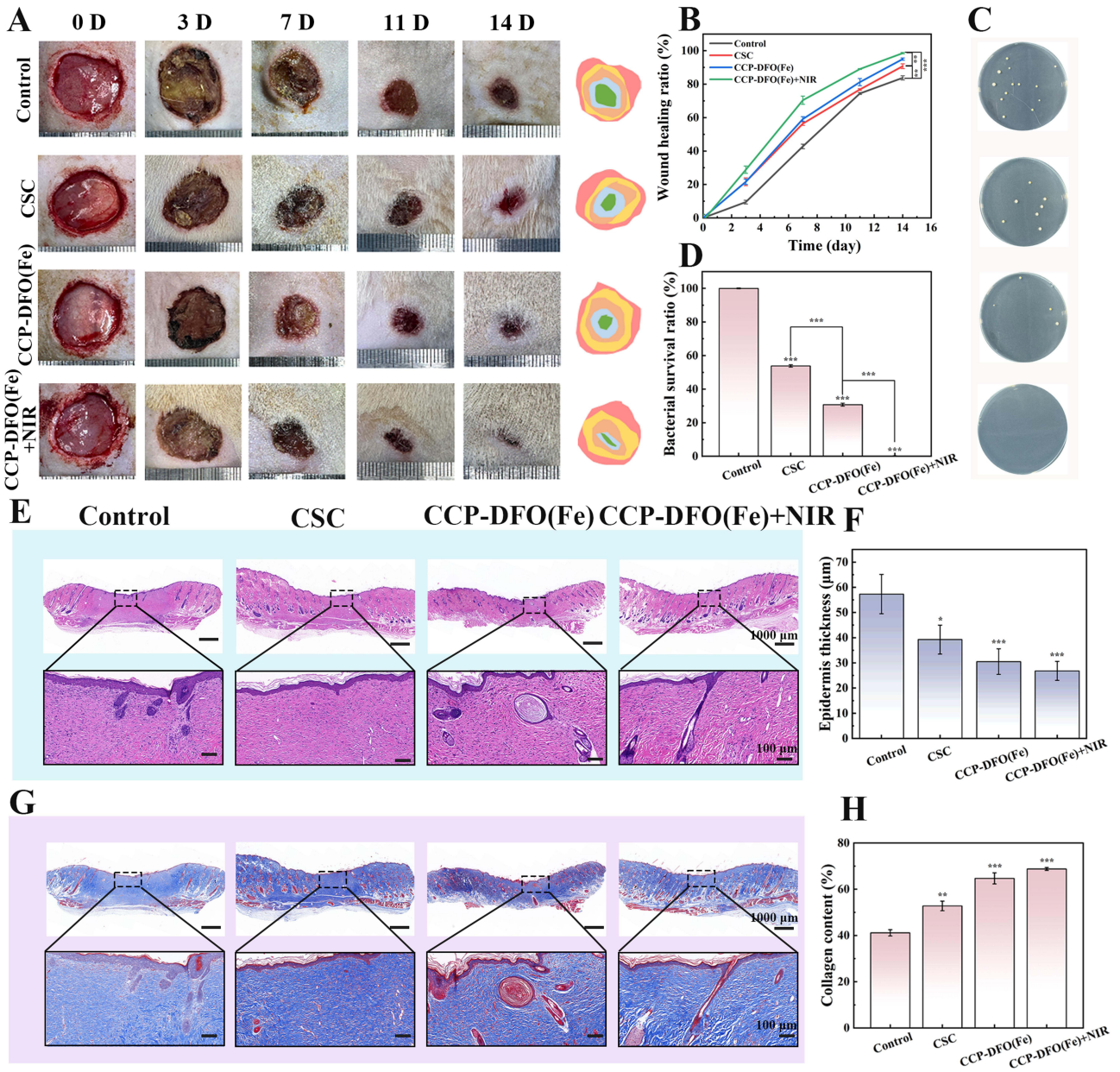

Figure 7 (**A**) Representative images of skin wounds monitored over 14 days following treatment with various materials. (**B**) Bacterial colony formation from wound sites at day 14. (**C**) Wound closure rates quantified over 14 days. (**D**) Bacterial survival rates at the wound site during the 14-day period. (**E**) H&E staining of wound sections at day 14. (**F**) Quantitative analysis of epidermal regeneration rate from H&E images. (**G**) Masson's trichrome staining showing collagen deposition. (**H**) Quantification of collagen content at day 14. (*p<0.05, **p<0.01, and ***p<0.001).

(Figures 7G, H and S12B). As a major component of the dermis, collagen deposition plays a critical role in wound repair. By day 14, collagen fibers in the control group appeared thin and disorganized, whereas the CSC group showed more abundant and denser collagen precipitation. Notably, the CCP-DFO(Fe) group presented clearly aligned collagen formation with further elevated deposition. NIR irradiation, which triggered the release of anti-inflammatory agents, protected fibroblasts from high ROS levels and further promoted collagen fiber production. Consequently, the CCP-DFO(Fe)+NIR group exhibited the most extensive and tightly arranged collagen network. Quantitative analysis confirmed that this group achieved the highest collagen content (68.75 ± 0.61%) at day 14, demonstrating the most enhanced wound-healing outcome.

To investigate the anti-inflammatory and macrophage-polarizing effects of CCP-DFO(Fe) nanoparticles during wound repair, further histological studies were performed. Neutrophil infiltration, a hallmark of acute inflammation, was evaluated by myeloperoxidase (MPO) immunohistochemical staining. As shown in Figure 8A, wound tissue in the

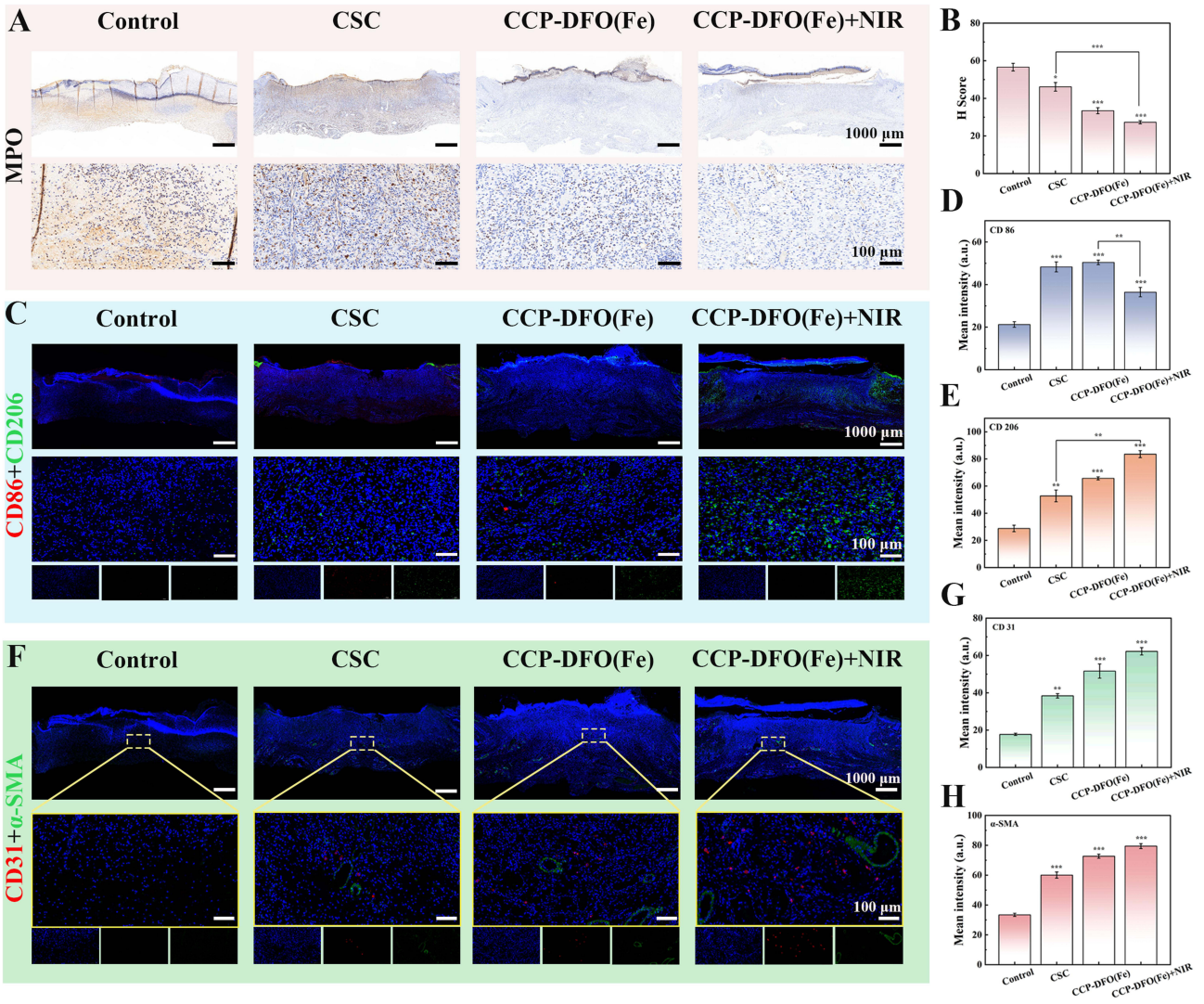

Figure 8 (**A**) Representative images of myeloperoxidase (MPO) immunohistochemical staining. (**B**) Quantitative H score analysis of MPO-positive staining. (**C**) Representative immunofluorescence images of CD86 (red, M1 marker) and CD206 (green, M2 marker) in full-thickness wounds at day 7. (**D**) Mean fluorescence intensity of CD86. (**E**) Mean fluorescence intensity of CD206. (**F**) Representative immunofluorescence images of α-SMA (green) and CD31 (red) in wound tissues on day 7. (**G**) Mean fluorescence intensity of CD31. (**H**) Mean fluorescence intensity of α-SMA. (*p<0.05, **p<0.01, and ***p<0.001).

control group exhibited extensive MPO-positive cells and diffuse extracellular staining, indicating severe acute inflammation. After CSC nanoparticle treatment, the staining background became clearer, with positive signals confined to distinct cytoplasmic granules. In contrast, the CCP-DFO(Fe)+NIR group showed markedly fewer MPO-positive cells, with weaker staining mainly localized around blood vessels. H Score quantitative analysis (Figure 8B) further confirmed that the CCP-DFO(Fe)+NIR group had a significantly lower H Score (27.28 ± 0.86) compared to the control (56.64 ± 2.03) and CSC (46.13 ± 2.32) groups (p<0.01). These results demonstrate that the combined bacterial targeting and photothermal therapy effectively attenuated acute inflammation characterized by neutrophil infiltration.

On day 7, wound tissue sections were subjected to dual immunofluorescence staining for CD86 (red, M1) and CD206 (green, M2) to evaluate the regulatory effect of the nanoparticles on macrophage phenotype. As shown in Figure 8C, the control group exhibited weak signals for both markers, suggesting that macrophages might be functionally suppressed or dysregulated under severe damage, failing to effectively initiate the healing program. In the CSC group, CD86 fluorescence increased compared to the control, indicating macrophage activation and a reduction in microenvironmental disturbance. The CCP-DFO(Fe) group showed no significant change in CD86 intensity relative to the CSC group (Figure 8D), which may be attributed to the slower release of CGA due to the PVCL encapsulation. In contrast, the CCP-DFO(Fe)+NIR group displayed

https://doi.org/10.2147/IJN.S594688

significantly reduced CD86 intensity and markedly enhanced CD206 signal (Figure 8E), demonstrating successful reprogramming of macrophages toward an anti-inflammatory phenotype. This effect is due to NIR-induced CGA release, which facilitates the shift from M1 to M2 macrophages, thereby shortening inflammation and promoting tissue repair. Overall, CCP-DFO(Fe)+NIR synergistically regulates macrophage polarization through photothermal action and controlled payload release, improving the local inflammatory environment and supporting wound healing.

The presence of neovascularization in wound tissue was assessed by immunofluorescence staining for CD31, a marker of vascular endothelium, and α-SMA, which labels actin stress fibers involved in wound contraction and repair.[52] As shown in the fluorescent images (Figure 8F) and quantitative analysis of CD31 (Figure 8G) and α-SMA (Figure 8H) intensity, the control group exhibited the lowest expression of both markers. While the CSC and CCP-DFO(Fe) groups showed comparable fluorescence levels, both were significantly higher than the control. The CCP-DFO(Fe)+NIR group showed the highest levels of CD31 and α-SMA staining. This suggests that NIR-activated CCP-DFO(Fe) enhances endothelial and myofibroblast activity, thereby facilitating neovascularization and supporting tissue remodeling and wound closure.

Taken together, this study developed a multifunctional nanoparticle system for treating bacterially infected wounds. The CCP-DFO(Fe) nanoparticle integrates a photothermal Cu_7S_4 core with the phenolic compound CGA, encapsulated in a thermosensitive PVCL shell that enables controlled release under NIR irradiation. Surface conjugation with DFO(Fe) further provides bacterial targeting through iron chelation. The resulting material exhibits strong antibacterial and antioxidant performance, good biocompatibility, and promotes wound healing by modulating inflammation, enhancing re-epithelialization, and stimulating angiogenesis.

Conclusion

In this study, a multifunctional smart nanoplatform (CCP-DFO(Fe)) was successfully constructed for photothermally triggered drug release and targeted delivery to promote the healing of bacterially infected wounds. Initially, Cu_7S_4 nanoparticles with excellent photothermal properties were synthesized, followed by electrostatic interaction with the natural antibacterial and anti-inflammatory polyphenol CGA to form CSC nanoparticles. Subsequently, the CSC nanoparticles were stably encapsulated by a thermosensitive PVCL shell, and DFO(Fe) was grafted onto the surface, resulting in a temperature-responsive smart nanoplatform with effective bacterial targeting ability. The phase transition of PVCL under NIR irradiation triggers the exposure and release of CGA and Cu_7S_4. The released CGA acts as the primary anti-inflammatory agent and coordinates anti-inflammatory and tissue-repair processes by scavenging ROS and inducing macrophage polarization toward the M2 phenotype. Concurrently, Cu_7S_4 releases Cu^{2+} to exert antibacterial effects and provides a stable photothermal effect that synergistically enhances the antibacterial activity. Experimental results demonstrated that the system exhibited a pronounced photothermal effect under NIR laser irradiation and maintained excellent photothermal stability over five irradiation cycles. It showed broad-spectrum antibacterial efficacy, reducing bacterial viability to below 5% against both *E. coli* and *S. aureus*, along with notable anti-biofilm capability. In the infected wound model, a 14-day treatment regimen using CCP-DFO(Fe)+NIR nanoparticles resulted in a 98.56 ± 1.08% wound closure rate, accompanied by nearly complete bacterial eradication. Histological analysis confirmed that the nanoparticles promoted epithelial regeneration, collagen deposition, macrophage reprogramming, and angiogenesis, thereby shortening the healing time and improving tissue remodeling. In summary, the CCP-DFO(Fe) nanoplatform holds broad application prospects for accelerating the healing of bacterially infected wounds.

Data Sharing Statement

The data that support the findings of this study are available from the corresponding author upon reasonable request.

Funding

This work was supported by the Health Research Project of Hunan Provincial Health Commission (Grant number: 20257724), the Open project of Provincial Key Laboratory of Union Hospital Affiliated to Fujian Medical University in 2021 (Grant No. XHZDSYS202103), the Xiamen medical and health guiding project (Grant No. 3502Z20224ZD1152), the Special funds for talent research start-up fund of First Affiliated Hospital of University of South China (Grant

No. 20210002-1007), the Guangzhou Basic and Applied Basic Research Foundation (2025A04J5261), and National Natural Science Foundation of China (32300962).

Disclosure

The authors declare no competing interest.

References

1. Ni D, Liu N, Peng Y, et al. MiR-181d-5p affects skin wound healing processes via the Ikbkg/NF-κB axis. *Int J Biol Macromol*. 2025;322:147007. doi:10.1016/j.ijbiomac.2025.147007
2. Huang K, Mi B, Xiong Y, et al. Angiogenesis during diabetic wound repair: from mechanism to therapy opportunity. *Burns Trauma*. 2025;13. doi:10.1093/burnst/tkae052
3. Bowler PG, Duerden BI, Armstrong DG. Wound microbiology and associated approaches to wound management. *Clin Microbiol Rev*. 2001;14 (2):244–269. doi:10.1128/cmr.14.2.244-269.2001
4. Mu W, Wang Y, Liu T, Zhang H, Weng L, Chen X. Nanocomposite hydrogel to integratively inhibit bacteria and inflammation for infected wound repair. *J Control Release*. 2025;386:114145. doi:10.1016/j.jconrel.2025.114145
5. Wang Y, luo M, Li T, Xie C, Li S, Lei B. Multi-layer-structured bioactive glass nanopowder for multistage-stimulated hemostasis and wound repair. *Bioact Mater*. 2023;25:319–332. doi:10.1016/j.bioactmat.2023.01.019
6. Qiao Y, He J, Chen W, et al. Light-activatable synergistic therapy of drug-resistant bacteria-infected cutaneous chronic wounds and nonhealing keratitis by cupriferous hollow nanoshells. *ACS Nano*. 2020;14(3):3299–3315. doi:10.1021/acsnano.9b08930
7. Sun M, Li D, Xi Y, et al. NIR-triggered bacterial cellulose-based wound dressings for multiple synergistic therapy of infected wound. *Int J Biol Macromol*. 2024;259:129033. doi:10.1016/j.ijbiomac.2023.129033
8. Lu S, Chen Z, Tu H, et al. Multifunctional carbon quantum dots decorated self-healing hydrogel for highly effective treatment of superbug infected wounds. *Chem Eng J*. 2024;480:148218. doi:10.1016/j.cej.2023.148218
9. Idrees T, Castro-Revoredo I, Dhatariya KK, Hernandez L, Umpierrez GE. Advances in the management of hyperglycaemia and diabetes mellitus during hospitalization. *Nat Rev Endocrinol*. 2025;21(12):757–768. doi:10.1038/s41574-025-01157-1
10. Yang Z-C, Lin H, Liu G-J, et al. CB-MNCs@ CS/HEC/GP promote wound healing in aged murine pressure ulcer model. *Stem Cell Res Ther*. 2025;16(1):52. doi:10.1186/s13287-025-04177-w
11. Lai L, Guo Q, Zou W, et al. Space-confined nanozyme with cascade reaction based on PCN-224 for synergistic bacterial infection treatment and NIR fluorescence imaging of wound bacterial infections. *Chem Eng J*. 2024;487:150642. doi:10.1016/j.cej.2024.150642
12. Wang Y, Chang F, Li Y, et al. Bi2WO6@Cu2O-GOx bio-heterojunctionp-n spray for accelerating chronic diabetic wound repairment with bilaterally enhanced sono-catalysis and glycolytic inhibition antisepsis. *Biomaterials*. 2025;317:123046. doi:10.1016/j.biomaterials.2024.123046
13. Pan Y, Fang L, Gu S, et al. Carbon dot decorated covalent organic framework for mild NIR-II photothermal and heterojunction amplified sonodynamic and chemodynamic therapy. *Carbon*. 2025;236:119987. doi:10.1016/j.carbon.2025.119987
14. Yang Y, Wang N, Wang Z, Yan F, Shi Z, Feng S. Glutathione-responsive metal–organic-framework-derived MnxOy/(A/R)TiO2 nanoparticles for enhanced synergistic sonodynamic/chemodynamic/immunotherapy. *ACS Nano*. 2025;19(1):885–899. doi:10.1021/acsnano.4c12304
15. Liu K, Zhao D, Zhao H, et al. Mild hyperthermia-assisted chitosan hydrogel with photothermal antibacterial property and CAT-like activity for infected wound healing. *Int J Biol Macromol*. 2024;254:128027. doi:10.1016/j.ijbiomac.2023.128027
16. Chen Y, Zhang C, Weng X, Jiang S, Cheng B. The impact of near-infrared-triggered photothermal therapy on collagen organization and wound healing. *J Photochemist Photobiol B*. 2025;272:113273. doi:10.1016/j.jphotobiol.2025.113273
17. Liu K, Zhang L, Lu H, et al. Enhanced mild-temperature photothermal therapy by pyroptosis-boosted ATP deprivation with biodegradable nanoformulation. *J Nanobiotechnol*. 2023;21(1):64. doi:10.1186/s12951-023-01818-1
18. Zhai S, You J, Yang Z, et al. Near-infrared light-responsive on-demand puerarin-releasing injectable hydrogel for promoting healing of infected wounds. *Mater Today Bio*. 2025;32:101817. doi:10.1016/j.mtbio.2025.101817
19. Peng W, Zhong Q, Zhang R, et al. Near-infrared light-responsive multifunctional hydrogel for synergistic photothermal/photodynamic/gas therapy to treat MRSA infections and accelerate wound healing. *J Colloid Interface Sci*. 2026;703:139168. doi:10.1016/j.jcis.2025.139168
20. Qiu D, Zheng C, Zeng Y, et al. Enzymolysis and photothermal-mediated synergistic antimicrobial nanoplatform with programmed EPS degradation and biofilm penetration capabilities for eradication of biofilm wound infections. *Chem Eng J*. 2023;477:147217. doi:10.1016/j.cej.2023.147217
21. Ma W, Chen X, Fu L, et al. Ultra-efficient antibacterial system based on photodynamic therapy and CO gas therapy for synergistic antibacterial and ablation biofilms. *ACS Appl Mater Interfaces*. 2020;12(20):22479–22491. doi:10.1021/acsami.0c01967
22. Lu H, He W, Li J, et al. Gas therapy in combating antimicrobial resistance: mechanisms, synergistic strategies, and clinical translation challenges. *Nano Today*. 2026;67:102960. doi:10.1016/j.nantod.2025.102960
23. Yan H, Dai C, Luan X, et al. Near-infrared light-responsive upconversion nanoparticles supported elemental selenium for combination tumor therapy: selenium therapy, photocatalytic therapy, and "AND" logic-gated chemotherapy. *ACS Appl Mater Interfaces*. 2025;17(24):36226–36239. doi:10.1021/acsami.5c08003
24. Wei D, Chen Y, Huang Y, et al. NIR-light triggered dual-cascade targeting core-shell nanoparticles enhanced photodynamic therapy and immunotherapy. *Nano Today*. 2021;41:101288. doi:10.1016/j.nantod.2021.101288
25. Zhang M, Song H, Feng Y, et al. A near-infrared light responsive nanoheterojunction for antibacterial and anti-inflammatory applications through programmed ROS regulation. *J Colloid Interface Sci*. 2025;700:138489. doi:10.1016/j.jcis.2025.138489
26. Yan S, Yu Z, Yang H, et al. Near-infrared light-triggered silk fibroin hydrogels integrated with polydopamine-modified nanoparticles for enhanced wound healing and infection control. *Int J Biol Macromol*. 2025;309:142814. doi:10.1016/j.ijbiomac.2025.142814
27. Wu X, Zhao G, Ruan Y, et al. Temperature-responsive nanoassemblies for self-regulated photothermal therapy and controlled copper release to accelerate chronic wound healing. *ACS Appl Bio Mater*. 2023;6(5):2003–2013. doi:10.1021/acsabm.3c00267

28. Zhou Y, Sun P, Cao Y, Yang J, Wu Q, Peng J. Biocompatible copper formate-based nanoparticles with strong antibacterial properties for wound healing. *J Nanobiotechnol*. 2023;21(1):474. doi:10.1186/s12951-023-02247-w
29. Cao B, Wu Z, Shen X, et al. EGCG/bimetallic organic framework modified titanium implants: harmonising anti-inflammatory and antioxidant responses to promote osteointegration. *Colloids Surf B*. 2025;254:114804. doi:10.1016/j.colsurfb.2025.114804
30. Chen M, He J, Xie S, et al. Intracellular bacteria destruction via traceable enzymes-responsive release and deferoxamine-mediated ingestion of antibiotics. *J Control Release*. 2020;322:326–336. doi:10.1016/j.jconrel.2020.03.037
31. Schalk IJ. Bacterial siderophores: diversity, uptake pathways and applications. *Nat Rev Microbiol*. 2025;23(1):24–40. doi:10.1038/s41579-024-01090-6
32. Tian K, Wu P, Gao S, et al. A deferoxamine-loaded microneedle patch enhances healing of radiation-induced skin injury: potential involvement of ferroptosis. *ACS Appl Mater Interfaces*. 2025;17(10):15035–15049. doi:10.1021/acsami.4c21589
33. Huang Q, Shan Q, Ma F, Li S, Sun P. Chlorogenic acid mitigates heat stress-induced oxidative damage in bovine mammary epithelial cells by inhibiting NF-κB-mediated NLRP3 inflammasome activation via upregulating the Nrf2 signaling pathway. *Int J Biol Macromol*. 2025;301:140133. doi:10.1016/j.ijbiomac.2025.140133
34. Zhang M, Wang Y, Yin X, et al. Chlorogenic acid-assisted dopamine-sodium alginate composite nanofiber membranes for promoting wound healing. *Carbohydr Polym*. 2025;354:123298. doi:10.1016/j.carbpol.2025.123298
35. Wang S, Liu Y, Wang X, et al. Modulating macrophage phenotype for accelerated wound healing with chlorogenic acid-loaded nanocomposite hydrogel. *J Control Release*. 2024;369:420–443. doi:10.1016/j.jconrel.2024.03.054
36. Ji Y, Tan H, Cheng X, et al. Targeting JAK2/STAT3-dependent macrophage polarization by chlorogenic acid attenuates hepatic inflammation in chronic stress. *Cells*. 2025;14(23):1848. doi:10.3390/cells14231848
37. Wang C, Zhang X, Zhuang Y, et al. Natural bioactive compounds solanesol and chlorogenic acid assembled nanomicelles for alzheimer's disease therapy. *ACS Appl Mater Interfaces*. 2025;17(9):14591–14603. doi:10.1021/acsami.4c22621
38. Fu X, Zhang H, Liu Z, Yu L, Zhang Y, Wang C. Right once for all: inflammation-targeted zinc–cobalt metal–organic framework nanozymes with high stability and broad-spectrum synergistic antibacterial properties for accelerating bacteria-infected wound healing under physiological conditions. *Small Struct*. 2025;6(8):2500068. doi:10.1002/sstr.202500068
39. Liu S, Wang H, He S, et al. Hydrothermal synthesis of chlorogenic acid-functionalized Ag nanoparticles and their antibacterial activity. *J Biomed Mater Res Part B*. 2025;113(8):e35616. doi:10.1002/jbm.b.35616
40. Yang M, Wang X, Ying B, et al. Multispectral-responsive Cu7S4@rGO bio-heterojunction for rapid sterilization through bacterial cuproptosis-like death. *Chem Eng J*. 2024;494:152809. doi:10.1016/j.cej.2024.152809
41. Mo S, Zhao Y, Wen J, et al. Efficient photothermal and photodynamic synergistic antibacterial therapy of Cu7S4 nanosheets regulated by facet engineering. *J Hazard Mater*. 2022;432:128662. doi:10.1016/j.jhazmat.2022.128662
42. Huang T, Guo Y, Wang Z, et al. Biomimetic dual-target theranostic nanovaccine enables magnetic resonance imaging and chemo/chemodynamic/immune therapy of glioma. *ACS Appl Mater Interfaces*. 2024;16(21):27187–27201. doi:10.1021/acsami.4c05831
43. Zhan M, Xu Y, Jia L, et al. Biomimetic copper-containing nanogels for imaging-guided tumor chemo-chemodynamic-immunotherapy. *Acta Biomater*. 2024;189:491–504. doi:10.1016/j.actbio.2024.09.030
44. Hua Y, Cao S, Yu Y, et al. A multifaceted nanodrug disrupts the copper–iron homeostasis to enhance cancer radiotherapeutic effect. *ACS Nano*. 2025;19(28):26091–26104. doi:10.1021/acsnano.5c06891
45. Fang G, Dong Q, Shen X, et al. Modulation of bacterial iron homeostasis to enhance cuproptosis-like death for the treatment of infected diabetic wound. *ACS Nano*. 2025;19(16):15578–15595. doi:10.1021/acsnano.4c17071
46. Conteh JS, Nucci GEP, Fernandez Cabada T, et al. CuFeS2 nanoparticles functionalized with a thermoresponsive polymer for photothermia and externally controlled drug delivery. *ACS Appl Mater Interfaces*. 2023;15(19):22999–23011. doi:10.1021/acsami.3c03902
47. Yang F, Wang N, Cui S, et al. Marine-inspired self-assembled peptide hydrogel spatiotemporal treatment of bacterial-infected wounds. *Chem Eng J*. 2025;519:165573. doi:10.1016/j.cej.2025.165573
48. Luo B, Bai X, Hou Y, et al. Research progress on MXenes in polysaccharide-based hemostasis and wound healing: a review. *Int J Biol Macromol*. 2025;303:140613. doi:10.1016/j.ijbiomac.2025.140613
49. Chen J, Zhang G, Zhao Y, Zhou M, Zhong A, Sun J. Promotion of skin regeneration through co-axial electrospun fibers loaded with basic fibroblast growth factor. *Adv Compos Hybrid Mater*. 2022;5(2):1111–1125. doi:10.1007/s42114-022-00439-w
50. Chen Y, Yin W, Liu Z, et al. Exosomes derived from fibroblasts enhance skin wound angiogenesis by regulating HIF-1α/VEGF/VEGFR pathway. *Burns Trauma*. 2025;13. doi:10.1093/burnst/tkae071
51. Li H-Y, Li M-Y, Cui C-X, et al. 4′-hydroxychalcone nanofiber hydrogel dressing promotes diabetic chronic wound healing by regulating macrophage polarization via the TLR/IL-17/TNF signaling pathway. *Mater Today Bio*. 2025;35:102474. doi:10.1016/j.mtbio.2025.102474
52. Chen S, Li Y, Ren S, et al. Amorphous zinc phosphate nanoclusters loaded polycarbonate thermosensitive hydrogel: an innovative strategy for promoting wound healing. *Mater Today Bio*. 2024;29:101266. doi:10.1016/j.mtbio.2024.101266